Technical Paper

Physically based real-time interactive assembly simulation of cable harness

Naijing Lv, Jianhua Liu*, Xiaoyu Ding, Jiashun Liu, Haili Lin, Jiangtao Ma

Beijing Institute of Technology, School of Mechanical Engineering, 5 South Zhongguancun Street, Haidian District, Beijing, 100081, China

ABSTRACT

In this paper, we designed and developed an interactive assembly simulation system of cable harness. First, we establish a real-time physical model of cable harness based on an extension of the mass–spring model. We use various kinds of springs to describe the different properties of the cable harness: linear springs for stretching, bending springs for bending, and torsion springs for geometrical torsion and material twisting. The constraints of connectors and clips on cable harness are both considered. We also associate the elastic coefficients of various springs with the material parameters of the cable. Moreover, we use spherical bounding volume hierarchy and triangular facets for collision detection of cable harness during the assembly simulation. By applying contact forces to both ends of the cable links that collide with the surrounding environment, we obtain the real-time contact response of the cable harness. Finally, we apply the proposed model to a cable assembly task. The results show that the proposed model successfully expressed the deformation of the cable harness and the interactive manipulation is computationally efficient.

© 2017 The Society of Manufacturing Engineers. Published by Elsevier Ltd. All rights reserved.

Introduction

Cable harnesses are used to connect electrical components, equipment, or control devices in complex products. They play important roles in transferring power and signals. The rationality of layout design and the reliability of cable assembly directly influence the performance of these products. In recent years, with the development of computer-aided design (CAD) and virtual reality (VR) technology, the routing design and assembly simulation of cable harness in virtual environment [1–8] has gradually attracted attention. For example, Ritchie et al. [4–6] developed an immersive VR system to design and plan the assembly and installation of cable harness. Valentini [7] and Liu et al. [8] implemented the interactive design of cable harness in augmented reality. Through simulation, we can verify the design rationality and assembly reliability of cables, then predict and solve the possible problems in their practical assembly in advance.

Modeling is the foundation of assembly simulation of cable harness in a virtual environment [9]. Any model of a cable must fulfill the demands of reality and real-time. On the one hand, it needs to express the real configurations and physical properties of cable harness. On the other, the calculation of the model needs to be sufficiently fast to keep up with assembly manipulation during the simulation process. The cable is a kind of deformable linear object (DLO). Recently, many researchers have developed models to simulate DLOs.

The dynamic spline model was first introduced to simulate deformable objects by Terzopoulos [10]. They combined the geometrical features of the spline with physical properties, such as mass and deformation energies. Lenoir et al. applied the idea of dynamic spline model to the manipulations of catheter and guidewire [11], as well as adaptive simulations [12]. Theetten et al. [13] provided geometrically exact dynamic splines and described a virtual system for cable positioning. Valentini et al. deduced a detailed dynamic spline formulation [14], and applied it to the interactive cable harnessing in augmented reality [7]. However, the computational time of this kind of model is relatively high when accounting for all of the physical properties.

The articulated link chain model [15] describes the DLO as consecutive rigid cylinder links connected by ball joints. Redon et al. [16] presented an adaptive algorithm for computing the forward dynamics of articulated bodies. Hergenröther et al. [17] equipped the joints with springs to express the bending behavior of cables, while Servin et al. [18] used a new type of "angular constraint." This kind of model is usually computed using inverse kinematics [19] or a minimal energy method [17]. However, because it con-
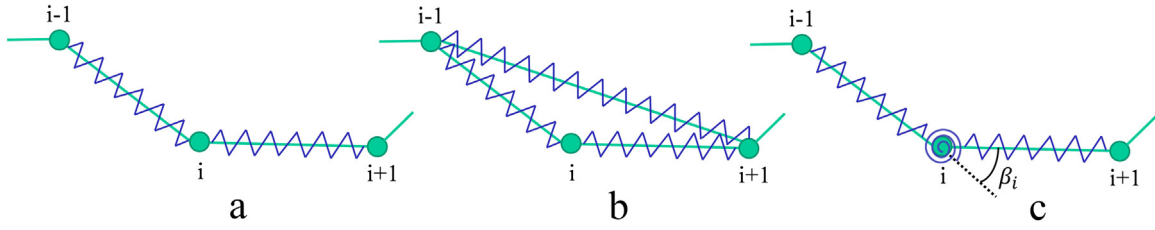
Fig. 1. Various mass-spring models in existing studies.

tains too few physical properties, the results provide only a limited description.

The finite element method (FEM) [20,21] can accurately express the deformations of cables, but the solving process is generally too complex and time-consuming to be usable for the real-time simulation of cables.

In recent years, several researchers have used an elastic rod model, which regards the DLO as a thin elastic rod. Two common methods are the Kirchhoff rod model and the Cosserat rod model. In 1859, Kirchhoff [22] proposed the dynamic analogy theory of an elastic thin rod. Bertails et al. [23] used the Kirchhoff equations to simulate human hair strands. Bergou et al. [24] and Bretl et al. [25] used the Kirchhoff elastic rod model to calculate the equilibrium configurations of DLOs under various manipulations. Cosserat's theory improved the Kirchhoff model by taking into account the axial linear strain and bending shear strain of the elastic rod, establishing more accurate equilibrium equations. Pai [26] first applied the Cosserat theory to the modeling of thin elastic solids. Spillmann et al. [27] and Grégoire et al. [28] used the Cosserat elastic rod model to simulate the bending and twisting behavior of one-dimensional flexible parts. The elastic rod model involves more comprehensive physical properties, but real-time simulation becomes a problem for high-complexity rods. It is also difficult to combine constraints with this model.

As a simple and real-time physical model, the mass–spring model is widely used in the simulation of flexible bodies, such as cloth [29,30], tissue [31], hair [32], and cable. This model was initially proposed by Haumann and Parant [33]. They described a behavioral simulation test-bed using particles connected by linear springs, as shown in Fig. 1(a). Provot et al. [29] improved the mass–spring model by adding "flexion springs," which are linear springs linking the masses i−1 and i+1, as shown in Fig. 1(b) and obtained good results in the simulation of the bending behavior of cloth. However, the disadvantage of the flexion spring is that for small angles, its length is almost constant, making the restoring force too small. To overcome this, Loock et al. [34] improved the model by using "torsion springs" attached to masses instead of the flexion springs, as shown in Fig. 1(c). They simulated the configuration of several cables with different material parameters under gravity and obtained a better bending effect of cables. However, existing mass-spring models did not consider the torsion deformation of the cable, which is very important to realistically express the deformation of a cable harness.

In this paper, we improved the usual mass–spring model by adding torsion springs to describe the twisting behavior of cable harness. We associated the elastic coefficients of springs with the material parameters of the cable for the first time. The practical constraints of connectors and clips on cable harness were also considered. Moreover, based on collision detection, we determined the real-time contact response of cable harness. Finally, based on the model, we developed an interactive assembly simulation system of cable harness and carried out an assembly task. The model successfully expressed the deformation of the cable harness and interactive manipulation was computationally efficient.

The paper is organized as follows. In Section 2, we introduce the real-time physical model of the cable harness. The collision detection and contact response of the model are introduced in Section 3. Section 4 presents the simulation results. Finally, the conclusions and future work are summarized in Section 5.

2. Physical modeling of cable harness

Previous mass–spring models only describe the gravity, stretching, and bending behaviors of cable harness. In this study, we added torsion springs to the model to describe twisting behavior, considered the constraints of connectors and clips on cable harness, and associated the elastic coefficients of springs with the material parameters of the cable. We then calculated the model based on quasi-static equilibrium conditions.

2.1. Description of the proposed model

The proposed model is shown in Fig. 2. The cable harness is modeled as a sequence of cable links consisting of discrete mass points and different springs. The various springs describes different physical properties of the cable harness. The linear springs connect every two adjacent mass points, expressing the stretching or compression behavior of the cable harness. Bending springs are attached to mass points that are not endpoints, to express the bending behavior of the cable harness. Additionally, we added torsion springs to the cable links to account for the geometric torsion and material twisting of the cable harness.

The basic notations are as follows:

(1) The cable harness is composed of n cable links (1,2,3...n) and n+1 mass points (0,1,2...n).
(2) m^0 is the total mass of the cable harness, and m_i is the mass of the point i. Each point has an equal mass, so $m_i = m^0/(n+1)$.
(3) l^0 is the initial total length of the cable harness and l_i^0 is the initial length of the cable link i. We assume that the initial length of each link is the same, so $l_i^0 = l^0/n$. l_i is the current length of cable link i.
(4) $\boldsymbol{x_i} = (x_i^1, x_i^2, x_i^3)^T$ is the three-dimensional coordinate of the mass point i in space, and ψ_i is the torsion angle of the cable link i.

2.2. Forces of the mass points

According to Newton's second law, we can determine the motion law of the mass points:

$$m_i \frac{\partial^2 \boldsymbol{x_i}}{\partial t^2} + k^d \frac{\partial \boldsymbol{x_i}}{\partial t} = \boldsymbol{F_i} = -\frac{\partial E}{\partial \boldsymbol{x_i}} + \boldsymbol{F_i^e}, \tag{1}$$

where k^d is the damping coefficient, preventing the excessive vibration of the mass points in the calculation process; $\boldsymbol{F_i}$ is the force acting on the point i; $\boldsymbol{F_i^i} = -\frac{\partial E}{\partial \boldsymbol{x_i}}$ and $\boldsymbol{F_i^e}$ are the internal and exter-
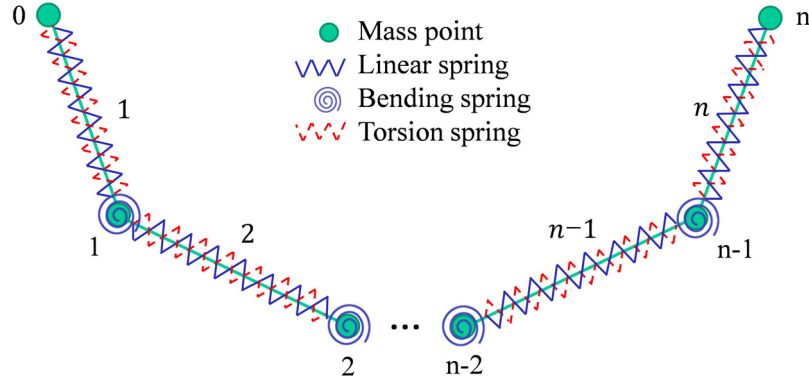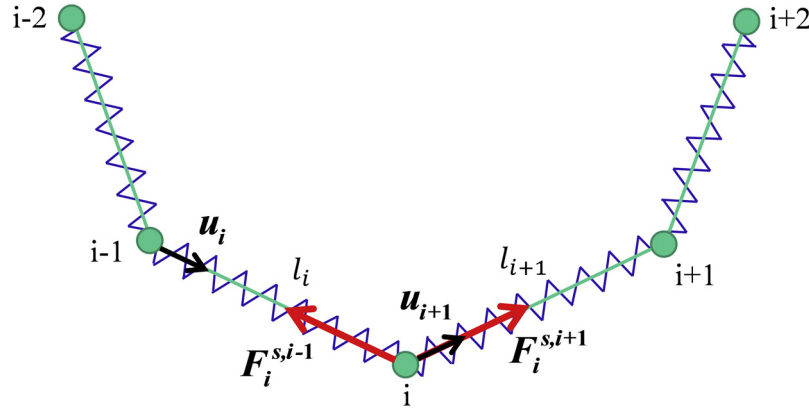
Fig. 2. Real-time physical model of cable harness.

Fig. 3. Stretching and compressing forces acting on mass point i.

nal force, respectively; $E = \sum\limits_{i=1}^{n} E_i$ is the potential energy of the spring system [34]. The internal force comes from the linear, bending and torsion springs, while the external force includes gravity, constraint force and other forces. The forces from the linear and bending springs have been introduced in Loock's work [34]. Here, we used the same idea and deduced the Eqs. (2)–(6).

2.2.1. Stretching and compressing force

The potential energy of the linear spring connecting the point i and $i-1$ is

$$E_i^s = k^s(l_i - l_i^0)^2/2 = k^s(|\boldsymbol{x_i} - \boldsymbol{x_{i-1}}| - l_i^0)^2/2, \tag{2}$$

where k^s is the elastic coefficient of the linear spring.

Thus the stretching or compressing force acting on the point i is

$$\boldsymbol{F_i^s} = -\frac{\partial E^s}{\partial \boldsymbol{x_i}} = -\left(\frac{\partial E_i^s}{\partial \boldsymbol{x_i}} + \frac{\partial E_{i+1}^s}{\partial \boldsymbol{x_i}}\right) = -k^s(l_i - l_i^0)\frac{\boldsymbol{x_i} - \boldsymbol{x_{i-1}}}{|\boldsymbol{x_i} - \boldsymbol{x_{i-1}}|} + k^s(l_{i+1} - l_{i+1}^0)\frac{\boldsymbol{x_{i+1}} - \boldsymbol{x_i}}{|\boldsymbol{x_{i+1}} - \boldsymbol{x_i}|}$$

$$= \underbrace{-k^s(l_i - l_i^0)\boldsymbol{u_i}}_{F_i^{s,i-1}} + \underbrace{k^s(l_{i+1} - l_{i+1}^0)\boldsymbol{u_{i+1}}}_{F_i^{s,i+1}}, \tag{3}$$

where $\boldsymbol{u_i}$ is the unit vector pointing from point $i-1$ to point i, that is used to indicate the direction of the forces.

The force $\boldsymbol{F_i^s}$ can be divided into $\boldsymbol{F_i^{s,i-1}}$ and $\boldsymbol{F_i^{s,i+1}}$, which are forces from the two linear springs that are connected to point i, as shown in Fig. 3.

2.2.2. Bending force

The potential energy of the bending spring attached to the point i is

$$E_i^b = k^b \beta_i^2/2, \tag{4}$$

where k^b is the elastic coefficient of the bending spring; β_i is the angle between the cable link i and $i+1$.

β_i can be expressed as

$$\beta_i = \arctan\left(\frac{|\boldsymbol{l_{i+1}} \times \boldsymbol{l_i}|}{\boldsymbol{l_{i+1}}^T \boldsymbol{l_i}}\right) = \arctan\left(\frac{|(\boldsymbol{x_{i+1}} - \boldsymbol{x_i}) \times (\boldsymbol{x_i} - \boldsymbol{x_{i-1}})|}{(\boldsymbol{x_{i+1}} - \boldsymbol{x_i})^T (\boldsymbol{x_i} - \boldsymbol{x_{i-1}})}\right), \tag{5}$$

where $\boldsymbol{l_i} = \boldsymbol{x_i} - \boldsymbol{x_{i-1}}$ is the vector pointing from point $i-1$ to point i.

Thus the bending force acting on the point i is

$$\boldsymbol{F_i^b} = -\frac{\partial E^b}{\partial \boldsymbol{x_i}} = -\left(\frac{\partial E_{i-1}^b}{\partial \boldsymbol{x_i}} + \frac{\partial E_i^b}{\partial \boldsymbol{x_i}} + \frac{\partial E_{i+1}^b}{\partial \boldsymbol{x_i}}\right) = -\left(k^b \beta_{i-1}\frac{\partial \beta_{i-1}}{\partial \boldsymbol{x_i}} + k^b \beta_i \frac{\partial \beta_i}{\partial \boldsymbol{x_i}} + k^b \beta_{i+1}\frac{\partial \beta_{i+1}}{\partial \boldsymbol{x_i}}\right)$$

$$= \underbrace{\frac{k^b \beta_{i-1}}{l_i}\frac{\boldsymbol{u_i} \times (\boldsymbol{u_{i-1}} \times \boldsymbol{u_i})}{\sin \beta_{i-1}}}_{F_i^{b,i-1}} - \underbrace{\frac{k^b \beta_i}{l_i}\frac{\boldsymbol{u_i} \times (\boldsymbol{u_i} \times \boldsymbol{u_{i+1}})}{\sin \beta_i}}_{F_i^{b,i,1} = -F_{i-1}^{b,i}} - \underbrace{\frac{k^b \beta_i}{l_{i+1}}\frac{\boldsymbol{u_{i+1}} \times (\boldsymbol{u_i} \times \boldsymbol{u_{i+1}})}{\sin \beta_i}}_{F_i^{b,i,2} = -F_{i+1}^{b,i}} + \underbrace{\frac{k^b \beta_{i+1}}{l_{i+1}}\frac{\boldsymbol{u_{i+1}} \times (\boldsymbol{u_{i+1}} \times \boldsymbol{u_{i+2}})}{\sin \beta_{i+1}}}_{F_i^{b,i+1}}.$$

$$\tag{6}$$
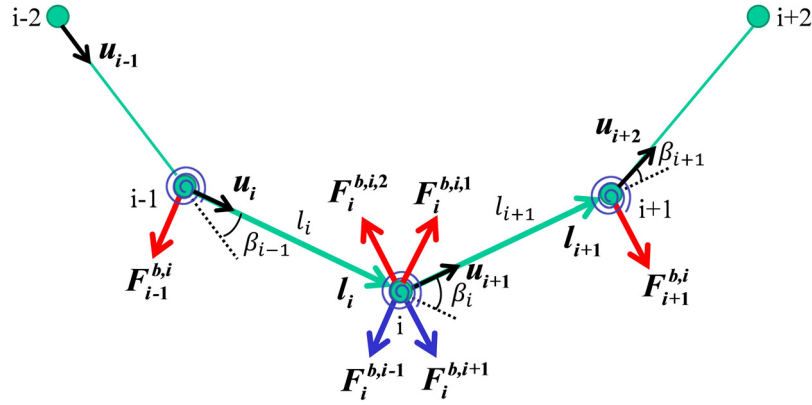
Fig. 4. Bending forces acting on mass point i.
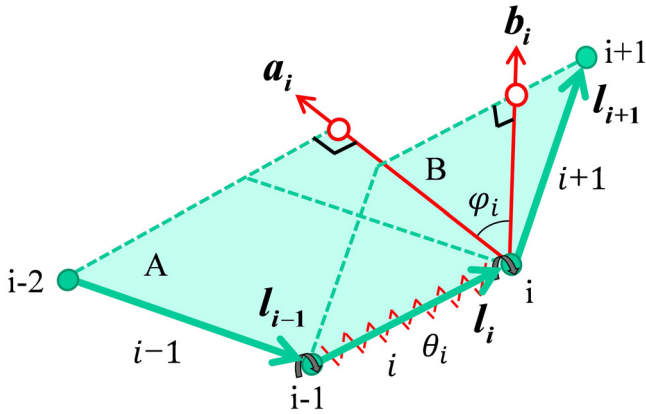
Fig. 5. Torsion angle of the cable link i.

The force $\boldsymbol{F_i^b}$ can be divided into $\boldsymbol{F_i^{b,i-1}}$, $\boldsymbol{F_i^{b,i,1}}$, $\boldsymbol{F_i^{b,i,2}}$ and $\boldsymbol{F_i^{b,i+1}}$, as shown in Fig. 4. $\boldsymbol{F_i^{b,i-1}}$ and $\boldsymbol{F_i^{b,i+1}}$ are the forces acting on point i from the bending springs attached to the points $i-1$ and $i+1$, while $\boldsymbol{F_i^{b,i,1}}$ and $\boldsymbol{F_i^{b,i,2}}$ are from the bending spring attached to point i. In other words, $\boldsymbol{F_{i-1}^{b,i}}$, $\boldsymbol{F_{i+1}^{b,i}}$, $\boldsymbol{F_i^{b,i,1}}$ $(=-\boldsymbol{F_{i-1}^{b,i}})$ and $\boldsymbol{F_i^{b,i,2}}$ $(=-\boldsymbol{F_{i+1}^{b,i}})$ are the forces of the bending spring attached to point i, and they form a balanced planar force system.

2.2.3. Twisting force

The torsion of a cable harness includes two parts: geometric torsion and material twisting [13,14]. The geometric torsion can be obtained with the coordinates of the mass points of the cable, while the material twisting is related to the relative twisting angle of the two ends of the cable. Thus, the potential energy of the torsion spring attached to the cable link i is

$$E_i^t = k^t \psi_i^2 / 2 = k^t \left(\varphi_i + \theta_i\right)^2 / 2, \tag{7}$$

where k^t is the elastic coefficient of the torsion spring; ψ_i is the total torsion angle of the cable link i; φ_i is the geometric torsion angle; θ_i is the material twisting angle.

As shown in Fig. 5, φ_i is the angle between the two osculating planes A and B. The plane A is determined by the two cable links $i-1$ and i, while B is determined by links i and $i+1$. $\boldsymbol{a_i}$ and $\boldsymbol{b_i}$ are the vectors that are perpendicular to the cable link i in the plane A and B, respectively. Thus φ_i can be expressed as

$$\varphi_i = \arctan\left(\frac{|\boldsymbol{a_i} \times \boldsymbol{b_i}|}{\boldsymbol{a_i}^T \boldsymbol{b_i}}\right), \tag{8}$$

where

$$\boldsymbol{a_i} = \boldsymbol{l_i} \times (\boldsymbol{l_i} \times \boldsymbol{l_{i-1}}) = (\boldsymbol{x_i} - \boldsymbol{x_{i-1}}) \times [(\boldsymbol{x_i} - \boldsymbol{x_{i-1}}) \times (\boldsymbol{x_{i-1}} - \boldsymbol{x_{i-2}})], \tag{9}$$

$$\boldsymbol{b_i} = \boldsymbol{l_i} \times (\boldsymbol{l_{i+1}} \times \boldsymbol{l_i}) = (\boldsymbol{x_i} - \boldsymbol{x_{i-1}}) \times [(\boldsymbol{x_{i+1}} - \boldsymbol{x_i}) \times (\boldsymbol{x_i} - \boldsymbol{x_{i-1}})]. \tag{10}$$

We assume that the material twisting of the cable is evenly distributed. The material twisting angle, θ_i, of each cable link can be expressed as

$$\theta_i = \frac{\theta}{n}, \tag{11}$$

where θ is the material twisting angle of the whole cable, which can be obtained by the rotations of the ends of the cable. θ_i is irrelevant to the positions of mass points, thus the twisting force acting on the point i is given by

$$\boldsymbol{F_i^t} = -\frac{\partial E^t}{\partial \boldsymbol{x_i}} = -\left(\frac{\partial E_{i-1}^t}{\partial \boldsymbol{x_i}} + \frac{\partial E_i^t}{\partial \boldsymbol{x_i}} + \frac{\partial E_{i+1}^t}{\partial \boldsymbol{x_i}} + \frac{\partial E_{i+2}^t}{\partial \boldsymbol{x_i}}\right) = -\left(k^t \psi_{i-1} \frac{\partial \varphi_{i-1}}{\partial \boldsymbol{x_i}} + k^t \psi_i \frac{\partial \varphi_i}{\partial \boldsymbol{x_i}} + k^t \psi_{i+1} \frac{\partial \varphi_{i+1}}{\partial \boldsymbol{x_i}} + k^t \psi_{i+2} \frac{\partial \varphi_{i+2}}{\partial \boldsymbol{x_i}}\right)$$

$$= \underbrace{-\frac{k^t \psi_{i-1}}{l_i \sin\beta_{i-1}} \frac{\boldsymbol{u_{i-1}} \times \boldsymbol{u_i}}{\sin\beta_{i-1}}}_{F_i^{t,i-1}} + \underbrace{\frac{k^t \psi_i}{l_{i+1} \sin\beta_i} \frac{\boldsymbol{u_i} \times \boldsymbol{u_{i+1}}}{\sin\beta_i}}_{F_i^{t,i,1}=-F_{i+1}^{t,i}} + \underbrace{\frac{k^t \psi_i}{l_i \tan\beta_i} \frac{\boldsymbol{u_i} \times \boldsymbol{u_{i+1}}}{\sin\beta_i}}_{F_i^{t,i,2}=-F_{i-1}^{t,i,3}} + \underbrace{\frac{k^t \psi_i}{l_i \tan\beta_{i-1}} \frac{\boldsymbol{u_{i-1}} \times \boldsymbol{u_i}}{\sin\beta_{i-1}}}_{F_i^{t,i,3}=-F_{i-1}^{t,i,2}}$$

$$\underbrace{-\frac{k^t \psi_{i+1}}{l_i \sin\beta_i} \frac{\boldsymbol{u_i} \times \boldsymbol{u_{i+1}}}{\sin\beta_i}}_{F_i^{t,i+1,1}} \underbrace{-\frac{k^t \psi_{i+1}}{l_{i+1} \tan\beta_i} \frac{\boldsymbol{u_i} \times \boldsymbol{u_{i+1}}}{\sin\beta_i}}_{F_i^{t,i+1,2}} \underbrace{-\frac{k^t \psi_{i+1}}{l_{i+1} \tan\beta_{i+1}} \frac{\boldsymbol{u_{i+1}} \times \boldsymbol{u_{i+2}}}{\sin\beta_{i+1}}}_{F_i^{t,i+1,3}} + \underbrace{\frac{k^t \psi_{i+2}}{l_{i+1} \sin\beta_{i+1}} \frac{\boldsymbol{u_{i+1}} \times \boldsymbol{u_{i+2}}}{\sin\beta_{i+1}}}_{F_i^{t,i+2}}. \tag{12}$$

For the sake of clarity and brevity, we only provide the final equation here. Please see the Appendix A for the specific derivation process.

Similar to the bending force, the twisting force $\boldsymbol{F_i^t}$ can be divided into eight components, as shown in Fig. 6. $\boldsymbol{F_i^{t,i-1}}$ and $\boldsymbol{F_i^{t,i+2}}$ are the
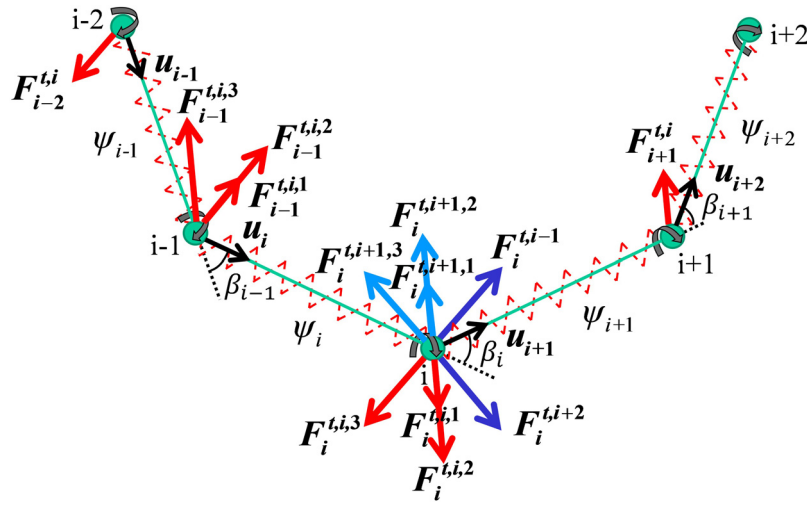
Fig. 6. Twisting forces acting on mass point i.

forces acting on point i from the torsion springs attached to cable links $i-1$ and $i+2$. $\boldsymbol{F}_i^{t,i,1}$, $\boldsymbol{F}_i^{t,i,2}$ and $\boldsymbol{F}_i^{t,i,3}$ are from the torsion spring attached to link i, while $\boldsymbol{F}_i^{t,i+1,1}$, $\boldsymbol{F}_i^{t,i+1,2}$ and $\boldsymbol{F}_i^{t,i+1,3}$ are from the spring $i+1$. In other words, $\boldsymbol{F}_{i-2}^{t,i}$, $\boldsymbol{F}_{i+1}^{t,i}$, $\boldsymbol{F}_{i-1}^{t,i,1}(=-\boldsymbol{F}_{i-2}^{t,i})$, $\boldsymbol{F}_{i-1}^{t,i,2}$, $\boldsymbol{F}_{i-1}^{t,i,3}$, $\boldsymbol{F}_i^{t,i,1}(=-\boldsymbol{F}_{i+1}^{t,i})$, $\boldsymbol{F}_i^{t,i,2}(=-\boldsymbol{F}_{i-1}^{t,i,3})$ and $\boldsymbol{F}_i^{t,i,3}(=-\boldsymbol{F}_{i-1}^{t,i,2})$ are the forces of the torsion spring attached to the link i, and they form a balanced spatial force system.

2.2.4. Gravity

Every point has mass; thus, it is affected by gravity:

$$\boldsymbol{G}_i = m_i \boldsymbol{g}. \tag{13}$$

2.2.5. Constraint force

In practice, cable harnesses are connected to electrical equipment through mechanical assemblies of electrical connectors. Connectors consist of sockets (female-ended) and plugs (male-ended), which are usually connected with equipment and cable harness, respectively. Moreover, in the process of cable wiring, we usually fix cable harnesses to appropriate positions using clips, preventing them from moving under external force or gravity. It also makes the arrangement of cable harness tidier and esthetic. Both connectors and clips have constraining effects on cable harness.

(1) Constraints of connectors

The ends of the cable harness 0 and n are usually connected with connectors, as shown in Fig. 7. Then, the positions of the ends are determined by that of the corresponding connectors. The torsion angle of the cable harness is related to the movement and rotation of the connectors.

Moreover, the connectors have directional constraints on the cable harness. Both ends of the cable harness tend to extend along the outlet directions of the connectors. To express the constraints, we add two constraining springs at the endpoints that are similar to but stiffer than the bending springs. The mass points 1 and $n-1$ will be affected by the corresponding spring.

$$\boldsymbol{F}_1^c = \frac{k^c \beta_0^*}{l_1} \frac{\boldsymbol{u}_1 \times (\boldsymbol{u}_0^* \times \boldsymbol{u}_1)}{\sin \beta_0^*}, \tag{14}$$

$$\boldsymbol{F}_{n-1}^c = \frac{k^c \beta_n^*}{l_n} \frac{\boldsymbol{u}_n \times (\boldsymbol{u}_{n+1}^* \times \boldsymbol{u}_n)}{\sin \beta_n^*}, \tag{15}$$

where k^c is the elastic coefficient of the constraining spring, which can be set to three times as big as k^b according to our experience;

$\boldsymbol{u}_0^*$ and $\boldsymbol{u}_{n+1}^*$ are the unit outlet direction vectors of the two connectors; β_0^* is the angle between $\boldsymbol{u}_0^*$ and $\boldsymbol{u}_1$, and β_n^* is the angle between $\boldsymbol{u}_{n+1}^*$ and $-\boldsymbol{u}_n$.

(2) Constraints of clips

Fig. 8 shows clip constraint in which the cable harness is fixed with a clip. $\boldsymbol{x}_i^*$ is the coordinate of the clip and on cable link i. The cable segment fixed by the clip can only move along with movement of the clip. To express this constraint, we remove the linear spring between mass points $i-1$ and i, and assume that the two points are located at the two ends of the clip.

$$\boldsymbol{x}_{i-1} = \boldsymbol{x}_i^* - (l_i^*/2)\,\boldsymbol{u}_i^*, \tag{16}$$

$$\boldsymbol{x}_i = \boldsymbol{x}_i^* + (l_i^*/2)\,\boldsymbol{u}_i^*, \tag{17}$$

where $\boldsymbol{u}_i^*$ is the unit outlet direction vector of the clip, and l_i^* is its length.

Similar to connectors, clips also add directional constraints to the cable harness. The constraints are expressed by the bending springs at points $i-1$ and i.

What's more, when colliding with the surrounding environment, the cable harness will be affected by contact forces. The details are respectively described in Section 3.

2.3. Coefficients determination

The elastic coefficients of various springs can be determined by the material parameters of the cable harness.

For a circular rod, assuming a length l_i, the section diameter is d, the Young's modulus of its material is E, and the Poisson's ratio is ν.

(1) Linear spring

When the circular rod is subjected to an axial force F^s, its axial deformation is given by

$$\Delta l = F^s l_i/(EA), \tag{18}$$

where EA is the stretching stiffness of the rod and A is its cross-sectional area, $A = \pi d^2/4$.

From Eq. (3), we can determine that for the same deformation, the force produced by the linear spring is
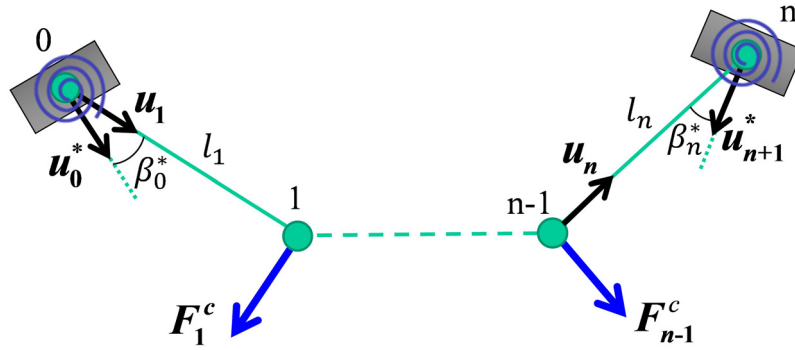
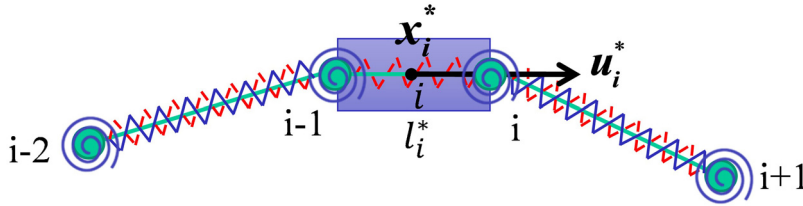$$F^s = k^s \Delta l. \tag{19}$$

Fig. 7. Constraints of connectors.

Fig. 8. Constraints of clips.

So the elastic coefficient of the linear spring k^s is

$$k^s = EA/l_i. \tag{20}$$

(2) Bending spring

The bending of the cable harness can be considered equivalent to a cantilever beam, as shown in Fig. 9. From Eq. (6), the bending force acting on point i from the bending spring attached to the point $i-1$ is

$$F_i^{b,i-1} = k^b \beta_{i-1}/l_i. \tag{21}$$

It means that $\boldsymbol{F^b}$, the force acting on point i from the cable segment behind point i, is opposite and equal to $\boldsymbol{F_i^{b,i-1}}$, so

$$F^b = F_i^{b,i-1}. \tag{22}$$

When the free end of the circular rod is subjected to a force F^b, its deflection is given by

$$\omega = F^b l_i^3 / (3EI) = l_i \beta_{i-1}, \tag{23}$$

where EI is the bending stiffness of the rod and I is the moment of inertia, $I = \pi d^4/64$.

So the elastic coefficient of the bending spring k^b is

$$k^b = 3EI/l_i. \tag{24}$$

(3) Torsion spring

When the circular rod is subjected to a torque T, the relative torsion angle of the two ends is

$$\psi = T l_i/(GI_p), \tag{25}$$

where GI_p is the twisting stiffness of the rod; G is the shear modulus of the rod material, and $G = E/2(1+\nu)$; I_p is the polar moment of inertia, and $I_p = \pi d^4/32$.

From Eq. (12), Figs. 5 and 6, we can determine that when the cable link i have the same torsion angle, the torsion of the torsion spring attached to the link i is

$$T = k^t \psi. \tag{26}$$

So the elastic coefficient of the torsion spring k^t is

$$k^t = GI_p/l_i. \tag{27}$$

2.4. Calculation of the model

In this study, the interactive assembly simulation process is based on a quasi-static assumption, and the two ends of the cable harness are assumed to be always held. The purpose of the calculation is to obtain the stable positions of all points of the cable harness at a given instant.

The calculation steps for the model are outlined as follows. For the first time solving the model, the cable harness should be divided equally into n links. The initial positions of all mass points are then determined. When the connector, clip, or any control point is moved, the rest of the points without constraints will move under the action of forces until reaching equilibrium. For convenience, we discretize time into a sequence of time steps, $\Delta\tau$, and use a simple Euler method [29]:

$$\begin{cases} \boldsymbol{a}_i^{\tau+\Delta\tau} = (\boldsymbol{F}_i^\tau - k^d \boldsymbol{v}_i^\tau)/m_i \\ \boldsymbol{v}_i^{\tau+\Delta\tau} = \boldsymbol{v}_i^\tau + \boldsymbol{a}_i^{\tau+\Delta\tau}\Delta\tau \\ \boldsymbol{x}_i^{\tau+\Delta\tau} = \boldsymbol{x}_i^\tau + \boldsymbol{v}_i^{\tau+\Delta\tau}\Delta\tau \end{cases} \tag{28}$$

Iterations of these calculations are performed until all points reach equilibrium; i.e., their accelerations and velocities approach zero. In this way, we determine the new, stable positions of all mass points.

The force of the mass point i is related to its position, which can be simply expressed as $\boldsymbol{F_i^\tau} = -K\boldsymbol{x_i^\tau}$. According to Eq. (28), we can deduce Eq. (29). The determinant of the matrix M in Eq. (29) is always less than 1, as shown in Eq. (30), which shows that the error decreases continually in the iteration process. It demonstrates that the method has convergence and numerical stability.

$$\begin{pmatrix} \boldsymbol{v_i} \\ \boldsymbol{x_i} \end{pmatrix}^{\tau+\Delta\tau} = M \begin{pmatrix} \boldsymbol{v_i} \\ \boldsymbol{x_i} \end{pmatrix}^\tau = \begin{bmatrix} 1 - \dfrac{k^d \Delta\tau}{m_i} & -\dfrac{K\Delta\tau}{m_i} \\ \Delta\tau - \dfrac{k^d \Delta\tau^2}{m_i} & 1 - \dfrac{K\Delta\tau^2}{m_i} \end{bmatrix} \begin{pmatrix} \boldsymbol{v_i} \\ \boldsymbol{x_i} \end{pmatrix}^\tau. \tag{29}$$
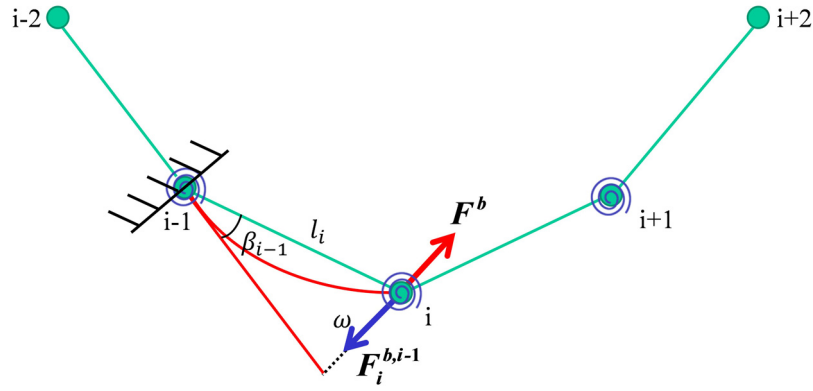
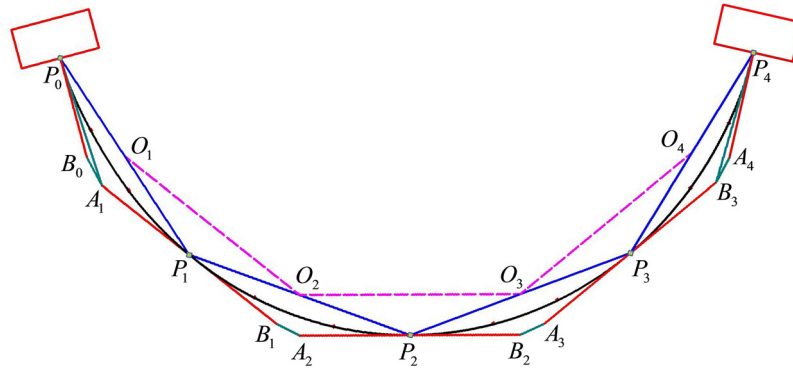**Fig. 9.** Coefficient determination of the bending spring.

Fig. 10. Piecewise Bézier curve fitting.

$$|M| = 1 - \frac{k^d \Delta \tau}{m_i} < 1. \tag{30}$$

However, the chosen of the time step $\Delta \tau$ here will affect the number of iterations for convergence by influencing the displacements of points for each step. Therefore, in order to avoid too many iterations are needed to reach equilibrium, we limit the maximum displacement of point, and assume that

$$\Delta \tau \approx \sqrt{(m_i l_i)/k}, \tag{31}$$

where k is the biggest elastic coefficient of various springs.

Additionally, the length of the cable harness can be calculated in real time using the curve interpolation method during the calculation process. When the length exceeds the ultimate tensile length, the calculation will stop, preventing further change of the cable's shape and/or length with assembly manipulation.

2.5. Piecewise Bézier curve fitting

After the stable positions of all mass points are obtained, we need to determine the smooth curve of the cable harness. We use the piecewise Bézier curve fitting method here. As shown in Fig. 10, P_i $(i=0,1\ldots,n)$ is the stable position of point; O_i is the midpoint of $P_{i-1}P_i$; A_iB_i is parallel and equal in length to O_iO_{i+1}, and P_i is the midpoint of A_iB_i; P_0B_0 and P_nA_n are the outlet direction of the connectors. Then the segment P_iP_{i+1} can be fitted with the cubic Bézier curve, which control polygon is $P_iB_iA_{i+1}P_{i+1}$. For cable harness without connectors, the end segments P_0P_1 and $P_{n-1}P_n$ can be fitted with the quadratic Bézier curves, which control polygons are $P_0A_1P_1$ and $P_{n-1}B_{n-1}P_n$, respectively. According to the property of Bézier curves that the curve is tangent to the first and last section

of the control polygon, the constructed curve would be smooth and look natural.

In this way, we can determine the stable configuration of the cable harness combining its section diameter. The system updates constantly, and the model computations require only a short time. Thus, complete cable deformation information is obtained efficiently upon simulation completion.

3. Collision detection and contact response

Fast and accurate collision detection and contact responses are essential in the assembly simulation of cable harness. Cables are deformable parts, and when contacting the surrounding environment, they will change their shapes to avoid penetration. Thus, not only should we detect whether a cable harness has collided with others but also obtain accurate collision information when a collision occurs and simulate the contact deformation response of the cable harness. Furthermore, the assembly simulation of cable harness needs interactive manipulation; thus, collision detection and contact response must be determined in real time.

3.1. Collision detection

Common methods of collision detection include bounding volume hierarchy (BVH), space decomposition, distance field method, image space, and an intelligent algorithm. Among them, BVH is one of the most common methods, and the bounding volume can be divided into the axis-aligned bounding box (AABB) [35], the oriented bounding box (OBB) [36], spheres [37], the discrete orientation polytope (K-DOP) [38], the convex hull [39], and other types.
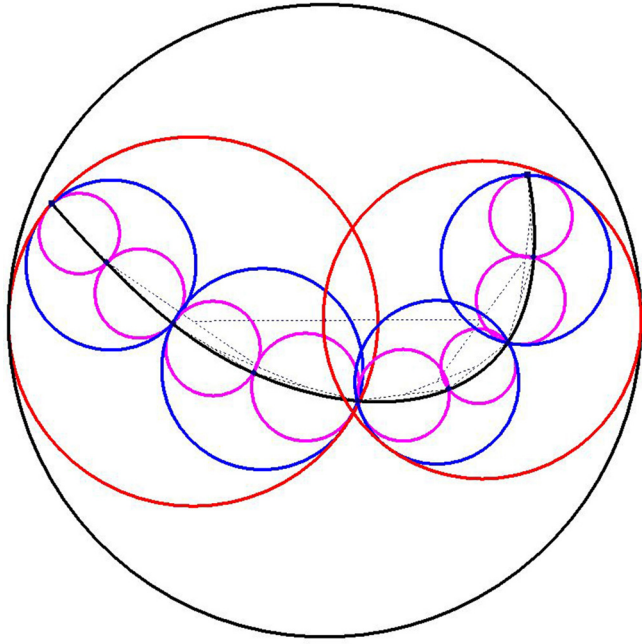
Fig. 11. Hierarchy tree of the cable harness.

The shape of the cable harness is always changing during the assembly simulation; thus, the collision model must be reconstructed in real time. In this study, we adopted the real-time spherical bounding volume hierarchy (SBVH) method. The hierarchy tree of the cable harness (Fig. 11) can be established and updated quickly from the bottom up.

The collision detection of SBVH is a top-down process. When the results show that some leaf nodes, or some bounding spheres surrounding some cable links, collide with something, the collision model of these cable links is reconstructed using triangular facets for accurate collision detection. Thus, we can know which links really collide with others, then return their numbers and the corresponding collision normal vectors.

3.2. Contact response

When a collision occurs, the cable harness will deform to avoid penetration, which is the contact response of it. In this study, we simulated the cable's contact response using a contact force-based method.

Cable link i collides with an object, and $\boldsymbol{n}$ is the collision normal direction (unit vector), as shown in Fig. 12. Then, link i will

be affected by contact forces from the object, including the normal support force and tangential friction force. For convenience of calculation, we transferred the contact force to the two end points, $i-1$ and i, of the link. Taking point i as an example, the force and velocity of it before the collision are $\boldsymbol{F_i}'$ and $\boldsymbol{v_i}'$, respectively. When a collision occurs, it will be affected by a support force $\boldsymbol{F_i^n}$ along the normal direction $\boldsymbol{n}$ first, which makes the normal components of $\boldsymbol{F_i}'$ and $\boldsymbol{v_i}'$ become zero. Thus,

$$\boldsymbol{F_i^n} = -\boldsymbol{F_i^{'n}} = -(\boldsymbol{F_i'} \cdot \boldsymbol{n}) \times \boldsymbol{n} = (\boldsymbol{F_i'} \cdot (-\boldsymbol{n})) \times \boldsymbol{n}, \tag{32}$$

$$\boldsymbol{v_i} = \boldsymbol{v_i'} - (\boldsymbol{v_i'} \cdot \boldsymbol{n}) \times \boldsymbol{n}. \tag{33}$$

The point moves in the tangent plane; thus, it will then be affected by a friction force, which can be obtained by the method of Xu et al. [40]. If v_i is not zero, the friction is a dynamic friction $\boldsymbol{F_i^{fd}}$. The magnitude of the dynamic friction equals the dynamic friction factor μ_d times the normal force F_i^n; its direction is opposite to the velocity of point $\boldsymbol{v_i}$.

$$\boldsymbol{F_i^{fd}} = -\mu_d F_i^n (\boldsymbol{v_i}/v_i). \tag{34}$$

If v_i is zero, or becomes zero due to energy loss, the friction will become a static friction $\boldsymbol{F_i^{fs}}$. The static friction is equal and opposite to $\boldsymbol{F_i^{'t}}$, the vector sum of $\boldsymbol{F_i'}$ and $\boldsymbol{F_i^n}$, or the tangential component of $\boldsymbol{F_i'}$. Thus, the force of the point becomes zero, and the point will be static.

$$\boldsymbol{F_i^{fs}} = -\boldsymbol{F_i^{'t}} = -(\boldsymbol{F_i'} + \boldsymbol{F_i^n}). \tag{35}$$

But when $F_i^{'t}$ exceeds the maximum static friction $F^{fs}_{\max}$, the product of the static friction factor μ_s and the normal force F_i^n, the point will move again and the friction will also become dynamic friction.

$$F_{\max}^{fs} = \mu_s F_i^n. \tag{36}$$

Furthermore, it is important to note that if the projection of $\boldsymbol{F_i'}$ or $\boldsymbol{v_i'}$ in the $\boldsymbol{n}$ direction is positive, then point i tends to leave the collision region. In this case, the contact force should be zero.

4. Results

Based on the physical model and collision handling above, we designed and developed an interactive assembly simulation system, in which we can operate and assemble cable harness interactively. The development and running environment of the system is shown in Table 1.
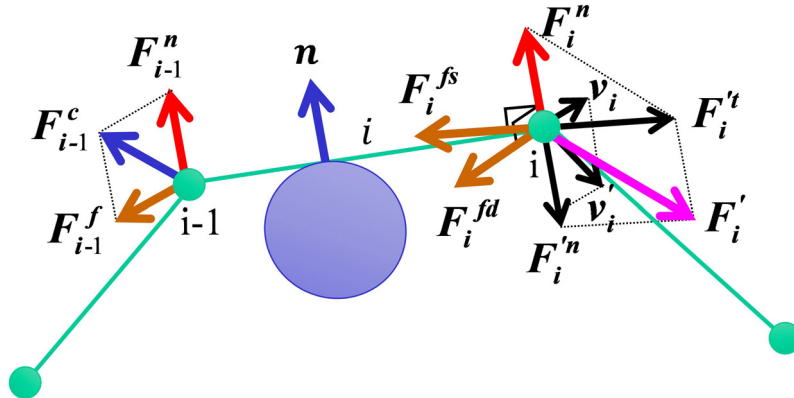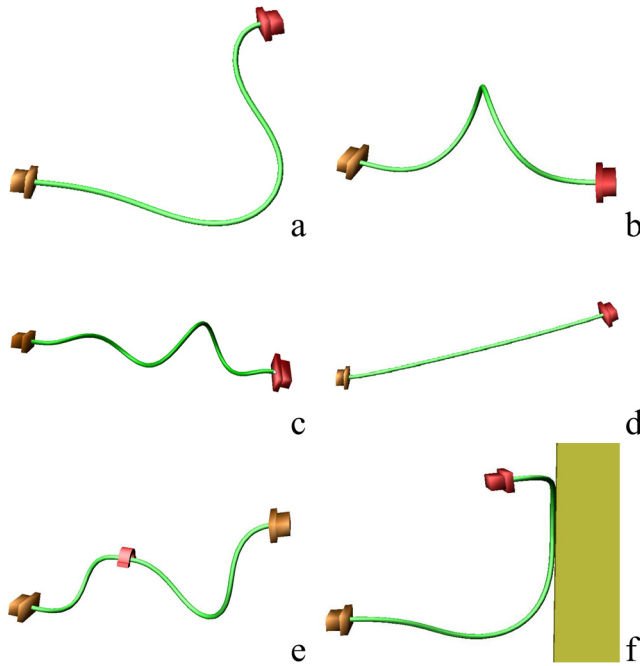

Fig. 12. Contact response of the cable harness.

Table 1
System environment.

System metrics	Detailed parameters
CPU	3.40 GHz Intel Core i7-3770 CPU
Graphics card	NVIDIA GeForce GTX 650 Ti
Memory	4 GB
Operating system	Windows 7
Development language	C/C++, XML, HTML

Table 2
Parameters of the cable harness.

Parameters	Value
Diameter d (mm)	4
Length l^0 (mm)	300
Total mass m^0 (g)	30
Young's modulus E (MPa)	126
Poisson's ratio ν	0.30
Dynamic friction factor μ_d	0.20
Static friction factor μ_s	0.30

Fig. 13. Deformation simulation of cable harness.

4.1. Simulation results and verification

4.1.1. Deformation simulation of the model

To confirm the proposed model, we simulated the deformation of cable harness under interactive manipulation. The simulation results are shown in Fig. 13.

When the ends of the cable harness or the connectors are moved or rotated, the cable harness will deform accordingly. Fig. 13(a–c) show different shapes of the cable, including bending and twisting behavior. The length of the cable harness is nearly constant during the entire process. Fig. 13(d) shows that when the distance between the two ends exceeds the ultimate ensile length of the cable harness, the connectors cannot be moved forward again. Fig. 13(e) shows the constraint of a clip. When the clip is moved or rotated, the cable harness will follow it and change its shape. Fig. 13(f) shows the deformation of the cable harness when colliding with another object.

From the graphs, we can see that the proposed model successfully expresses the deformation of the cable harness. Collisions can be detected effectively and the cable will deform accordingly to prevent penetration.

4.1.2. Experimental verification

To verify the reality of the proposed model, we measured a cable harness and compared the simulation results to the real world experiments. The material parameters of the cable harness and other parameters used in the model are shown in Table 2. The contrast results are shown in Figs. 14 and 15.

Fig. 14 shows the deformations of the cable harness during the process that the left end of it closes the right one gradually after

rotating about 0°(a), 180°(b) and 720°(c), respectively. Fig. 15 show the deformation of the cable harness when colliding with other objects. Fig. 15(a) shows the process that the right end of the cable harness and then the left one drops to the tabletop, and eventually hangs on the edge of the table. Fig. 15(b) shows the process that the right end of the cable harness lying on the tabletop rotates and closes the left one gradually.

From the graphs, we can see that the deformations of the cable harness in simulations are in good agreement with that in experiments. The proposed model can describe the deformation of the cable harness accurately, and the effects of collision detection and contact responses are also realistic.

4.1.3. Comparison with the finite element model

The experimental verification above is a qualitative evaluation, which is not sufficient, and more precise comparison is necessary. Therefore, we compared the proposed model to the finite element model to achieve a quantitative assessment. For the finite element method, the cable harness is modeled with a structured mesh of 15584 solid hexahedral element with 8 node for each. The model and the mesh details are depicted in Fig. 16. The parameters used in the models are the same as above.

During the simulation, the left end of the cable harness was fixed, while displacements and torsions were applied to the right end. Fig. 17 shows the projections of the cable's spatial shapes calculated by the two models on three coordinate planes. There are three groups of data with different distances and relative torsion angles between the two ends of the cable, as shown in the picture.

By comparison, the differences between the two models are limited within 3.3 mm (the total length of the cable harness is 300 mm), which means that the proposed model can simulate the deformation of the cable harness accurately.

4.2. Real-time performance of the model

The authenticity of the Cosserat model has been recognized by many researchers, because it can include enough physical properties of cables [26–28]. By comparison with the Cosserat model, we found that our model has better real time performance with the similar authenticity, which demonstrates the efficiency of our algorithm. To demonstrate this advantage, we tested the average computation time of the two models with different number of mass points on the same computer. The results are shown in Fig. 18.

From the figure, we can see that the computation time increased almost linearly with the number of mass points. Moreover, it is easy to see that the calculation speed of our model is faster than that of the Cosserat model.

In interactive simulations, the refresh rate must be more than 30 fps to guarantee the fluency of the manipulation; that is, the time of each calculation has to be less than 33 ms, which corresponds to 80 points for our model. Thus, as long as the number of mass points is less than 80, our model can satisfy the real-time requirement for interactive assembly simulation.
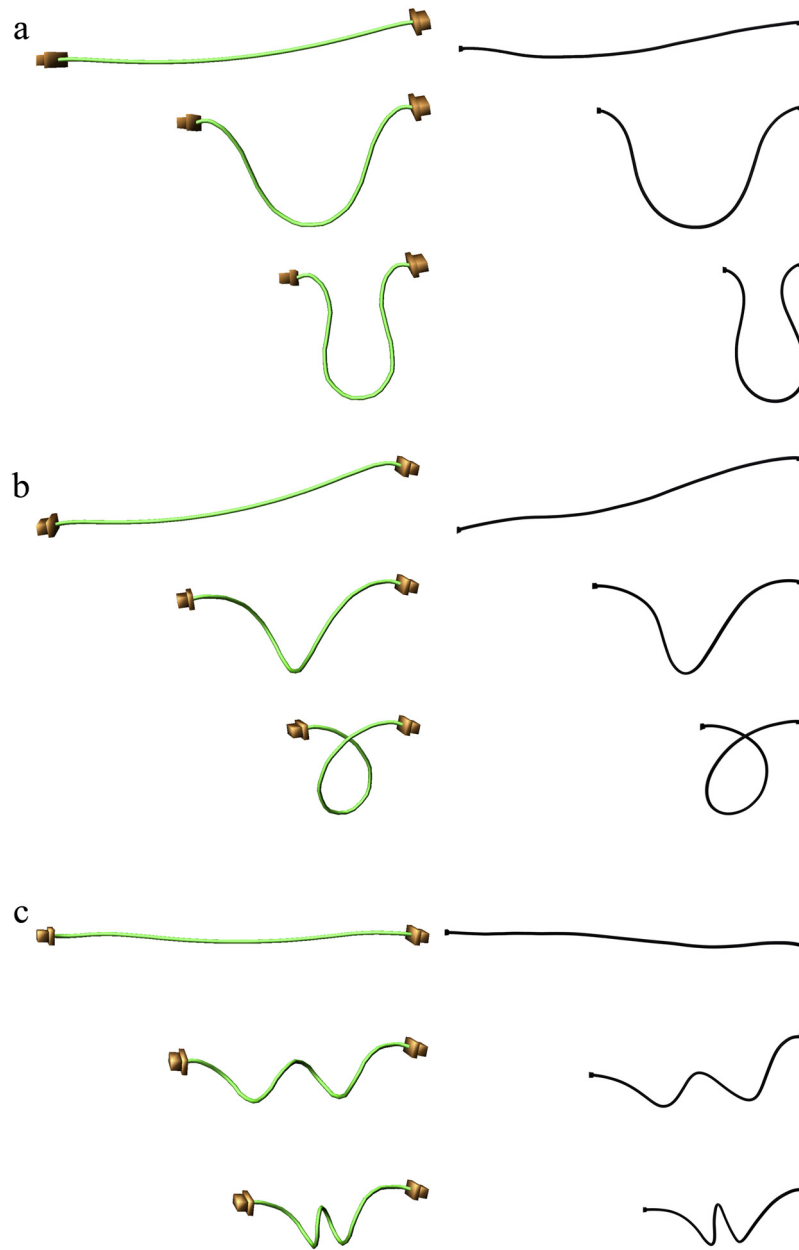
Fig. 14. Experimental verification of cable deformation.

For a specific cable harness, the decrease in the number of mass points means that the initial length of each cable link l_i^0 increases, which will lead to the decrease of the accuracy of the model. However, if l_i^0 is too small, the computation efficiency will be negatively affected. Therefore, in practice, the number of mass points and the length of each cable link should be determined according to the total length of the cable harness and the specific requirements. In the current case study, it has been shown that both the accuracy and efficiency of the model are satisfactory when l_i^0 is between 5 and 30 mm.

4.3. Assembly simulation of cable harness

To confirm the reliability of the system, we carried out an application example of a cable's interactive assembly simulation. As shown in Fig. 19, the socket connector B01-X3 is the third connector on the electric equipment B01, while C02-X7 is the seventh connector on equipment C07. The assembly task is to insert the two plug connectors connected with the cable harness into the two socket connectors B01-X3 and C02-X7 respectively.

The assembly process is as follows:

(a) Import the required CAD models into the system.
(b) Operate the whole cable harness near the installation site.
(c) Operate one plug connector connected with the cable harness and insert it into the socket connector B01-X3. The cable harness collides with another part (arrow) in the process, and the cable harness deforms to avoid penetration.
(d) Operate the other plug connector and insert it into the socket connector C02-X7.
(e) Operate the control points, and position the cable harness close to the surfaces of parts.
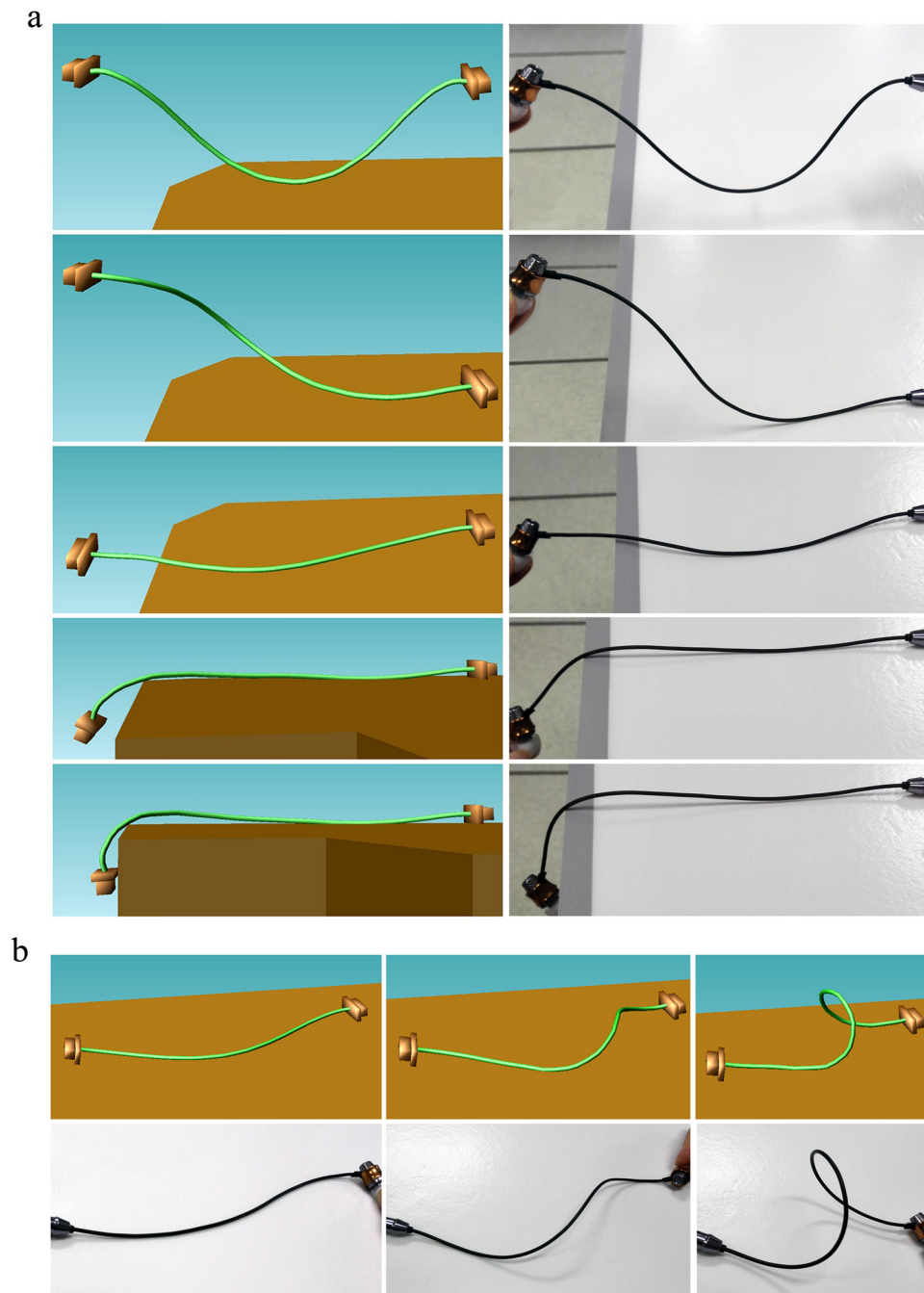(f) Install the clips and adjust their positions. The cable harness assembly is now complete.

a

b

Fig. 15. Experimental verification of collision and contact.
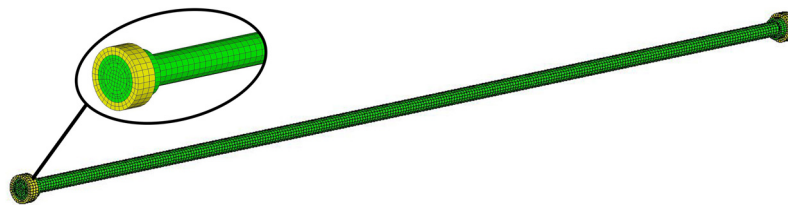

Fig. 16. The finite element method.

From the example, we can see that the simulation system successfully simulated the deformation of the cable harness in the interactive assembly process and that the interactive manipulation was computationally efficient.

5. Conclusions and future work

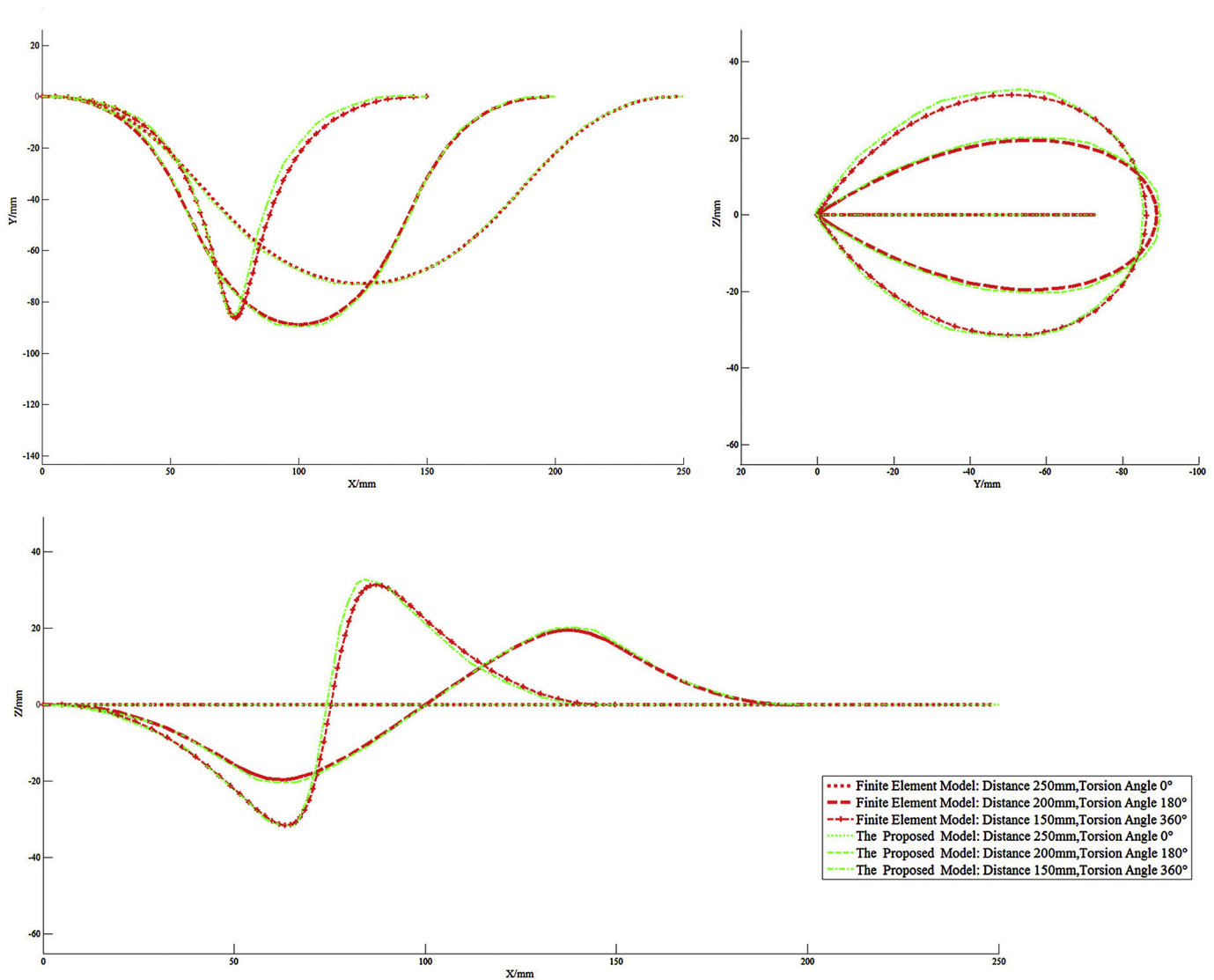In this paper, we present a method for the real-time interactive assembly simulation of cable harness based on an extension

Fig. 17. Comparison with the finite element model.

of the mass–spring model. We improved the usual mass–spring model by adding torsion springs attached to the cable links to express twisting behavior, including geometrical torsion and material twisting. And we associated the elastic coefficients of springs with the material parameters of the cable for the first time. The practical constraints of connectors and clips on the cable harness were also described by adding or removing springs.

Moreover, based on fast, accurate collision detection, we successfully simulated the cable's contact responses using a contact force-based method. By applying contact forces (including normal support forces and tangential friction forces) to both ends of the cable links that collide with surrounding environments, we simulated the deformation of the cable harness to avoid penetration.

At present, the simulation of cable harness is assumed to be quasi-static, because we believe that a quasi-static simulation, though not as realistic as a dynamic one, can be very efficient. Thus it is believed to be more suitable for the applications of interactive assembly of complex cables. In future researches, we will further improve the accuracy of collision detection and the effect of contact response, to adapt to more complex assembly environment. What's more, the physical modeling of branch cable harness is also a meaningful subject.
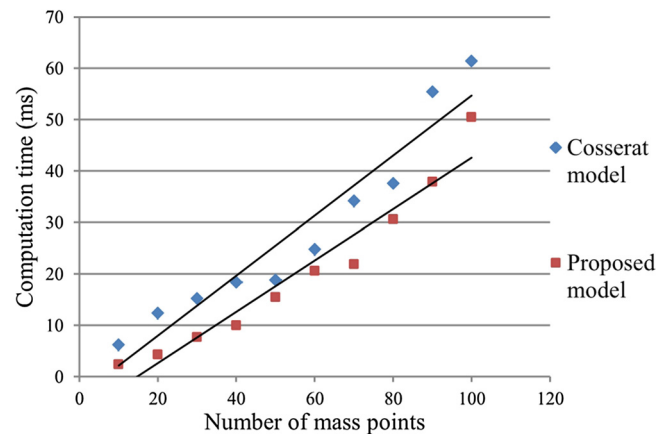

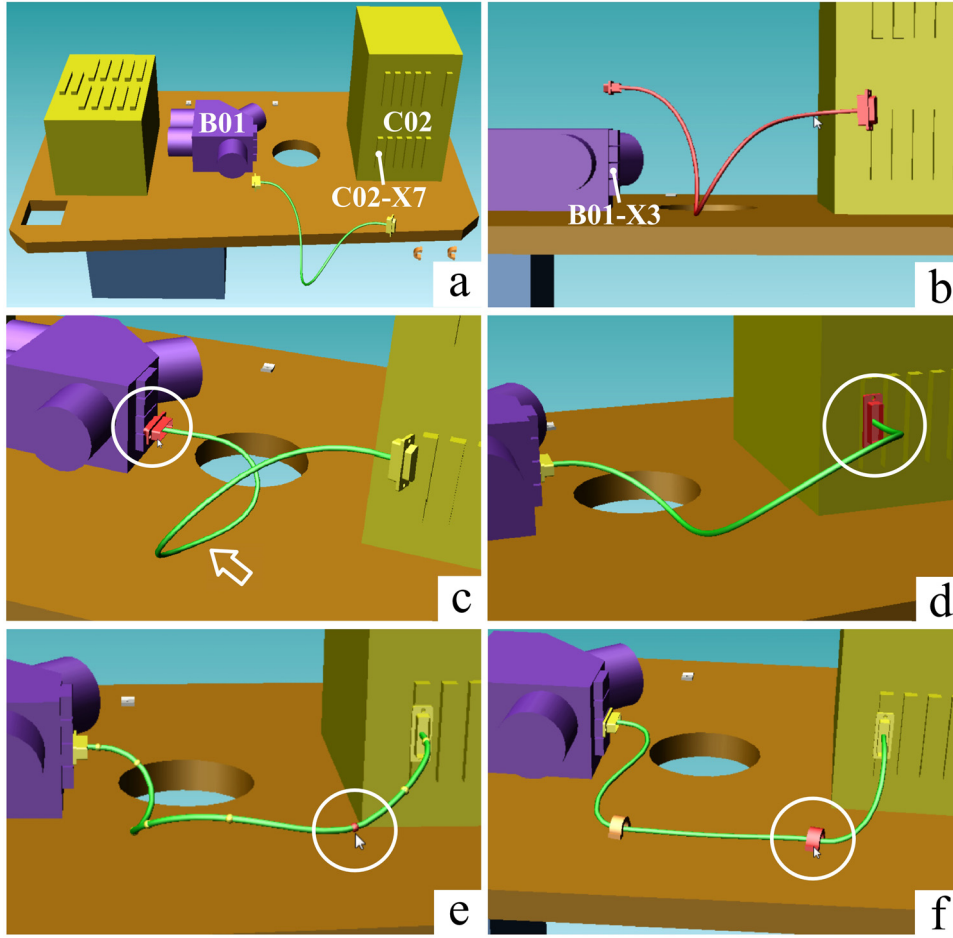**Fig. 18.** Comparison of calculation time.

Acknowledgments

Fig. 19. Interactive assembly simulation of cable harness.

Appendix A.

The potential energy of the torsion spring attached to the cable link i is

$$E_i^t = k^t \psi_i^2 / 2 = k^t(\varphi_i + \theta_i)^2 / 2. \tag{37}$$

φ_i can be expressed as

$$\varphi_i = \arctan(\frac{|\boldsymbol{a_i} \times \boldsymbol{b_i}|}{\boldsymbol{a_i}^T \boldsymbol{a_i}}), \tag{38}$$

where

$$\boldsymbol{a_i} = \boldsymbol{l_i} \times (\boldsymbol{l_i} \times \boldsymbol{l_{i-1}}) = (\boldsymbol{l_i}^T \boldsymbol{l_{i-1}})\boldsymbol{l_i} - (\boldsymbol{l_i}^T \boldsymbol{l_i})\boldsymbol{l_{i-1}} = (\boldsymbol{x_i} - \boldsymbol{x_{i-1}}) \times [(\boldsymbol{x_i} - \boldsymbol{x_{i-1}}) \times (\boldsymbol{x_{i-1}} - \boldsymbol{x_{i-2}})] \tag{39}$$

$$\boldsymbol{b_i} = \boldsymbol{l_i} \times (\boldsymbol{l_{i+1}} \times \boldsymbol{l_i}) = (\boldsymbol{l_i}^T \boldsymbol{l_i})\boldsymbol{l_{i+1}} - (\boldsymbol{l_i}^T \boldsymbol{l_{i+1}})\boldsymbol{l_i} = (\boldsymbol{x_i} - \boldsymbol{x_{i-1}}) \times [(\boldsymbol{x_{i+1}} - \boldsymbol{x_i}) \times (\boldsymbol{x_i} - \boldsymbol{x_{i-1}})]. \tag{40}$$

Thus the twisting force acting on the point i is

$$\boldsymbol{F_i^t} = -\frac{\partial E^t}{\partial \boldsymbol{x_i}} = -\left(\frac{\partial E_{i-1}^t}{\partial \boldsymbol{x_i}} + \frac{\partial E_i^t}{\partial \boldsymbol{x_i}} + \frac{\partial E_{i+1}^t}{\partial \boldsymbol{x_i}} + \frac{\partial E_{i+2}^t}{\partial \boldsymbol{x_i}}\right) = -\left(k^t \psi_{i-1} \frac{\partial \varphi_{i-1}}{\partial \boldsymbol{x_i}} + k^t \psi_i \frac{\partial \varphi_i}{\partial \boldsymbol{x_i}} + k^t \psi_{i+1} \frac{\partial \varphi_{i+1}}{\partial \boldsymbol{x_i}} + k^t \psi_{i+2} \frac{\partial \varphi_{i+2}}{\partial \boldsymbol{x_i}}\right), \tag{41}$$

where

$$
\frac{\partial \varphi_i}{\partial x_i} = \frac{\partial \mathbf{a}_i}{\partial x_i}\frac{\partial \varphi_i}{\partial \mathbf{a}_i} + \frac{\partial \mathbf{b}_i}{\partial x_i}\frac{\partial \varphi_i}{\partial \mathbf{b}_i} = \left(\frac{\partial \mathbf{l}_i}{\partial x_i}\frac{\partial \mathbf{a}_i}{\partial \mathbf{l}_i}\right)\frac{\partial \varphi_i}{\partial \mathbf{a}_i} + \left(\frac{\partial \mathbf{l}_i}{\partial x_i}\frac{\partial \mathbf{b}_i}{\partial \mathbf{l}_i} + \frac{\partial \mathbf{l}_{i+1}}{\partial x_i}\frac{\partial \mathbf{b}_i}{\partial \mathbf{l}_{i+1}}\right)\frac{\partial \varphi_i}{\partial \mathbf{b}_i} = \frac{\partial \mathbf{a}_i}{\partial \mathbf{l}_i}\frac{\partial \varphi_i}{\partial \mathbf{a}_i} + \frac{\partial \mathbf{b}_i}{\partial \mathbf{l}_i}\frac{\partial \varphi_i}{\partial \mathbf{b}_i} - \frac{\partial \mathbf{b}_i}{\partial \mathbf{l}_{i+1}}\frac{\partial \varphi_i}{\partial \mathbf{b}_i}
$$

$$
= \frac{\partial \mathbf{a}_i}{\partial \mathbf{l}_i}\frac{\mathbf{a}_i \times (\mathbf{a}_i \times \mathbf{b}_i)}{\mathbf{a}_i{}^2 |\mathbf{a}_i \times \mathbf{b}_i|} + \frac{\partial \mathbf{b}_i}{\partial \mathbf{l}_i}\frac{\mathbf{b}_i \times (\mathbf{b}_i \times \mathbf{a}_i)}{\mathbf{b}_i{}^2 |\mathbf{a}_i \times \mathbf{b}_i|} - \frac{\partial \mathbf{b}_i}{\partial \mathbf{l}_{i+1}}\frac{\mathbf{b}_i \times (\mathbf{b}_i \times \mathbf{a}_i)}{\mathbf{b}_i{}^2 |\mathbf{a}_i \times \mathbf{b}_i|}
$$

$$
= (\mathbf{l}_i{}^T \mathbf{l}_{i-1} + \mathbf{l}_{i-1} \mathbf{l}_i{}^T - 2\mathbf{l}_i \mathbf{l}_{i-1}{}^T)\frac{\mathbf{l}_i \times \mathbf{l}_{i-1}}{l_i{}^3 l_{i-1}{}^2 \sin^2 \beta_{i-1}} + (2\mathbf{l}_i \mathbf{l}_{i+1}{}^T - \mathbf{l}_i{}^T \mathbf{l}_{i+1} - \mathbf{l}_{i+1} \mathbf{l}_i{}^T)\frac{\mathbf{l}_i \times \mathbf{l}_{i+1}}{l_i{}^3 l_{i+1}{}^2 \sin^2 \beta_i} - (\mathbf{l}_i{}^T \mathbf{l}_i - \mathbf{l}_i \mathbf{l}_i{}^T)\frac{\mathbf{l}_i \times \mathbf{l}_{i+1}}{l_i{}^3 l_{i+1}{}^2 \sin^2 \beta_i}
$$

$$
= \frac{\mathbf{l}_i \times \mathbf{l}_{i-1}}{l_i{}^2 l_{i-1} \sin \beta_{i-1} \tan \beta_{i-1}} - \frac{\mathbf{l}_i \times \mathbf{l}_{i+1}}{l_i{}^2 l_{i+1} \sin \beta_i \tan \beta_i} - \frac{\mathbf{l}_i \times \mathbf{l}_{i+1}}{l_i l_{i+1}{}^2 \sin^2 \beta_i} = \frac{\mathbf{u}_i \times \mathbf{u}_{i-1}}{l_i \sin \beta_{i-1} \tan \beta_{i-1}} - \frac{\mathbf{u}_i \times \mathbf{u}_{i+1}}{l_i \sin \beta_i \tan \beta_i} - \frac{\mathbf{u}_i \times \mathbf{u}_{i+1}}{l_{i+1} \sin^2 \beta_i},
$$

$$
\tag{42}
$$

$$
\frac{\partial \varphi_{i+1}}{\partial x_i} = \frac{\partial a_{i+1}}{\partial x_i}\frac{\partial \varphi_{i+1}}{\partial a_{i+1}} + \frac{\partial b_{i+1}}{\partial x_i}\frac{\partial \varphi_{i+1}}{\partial b_{i+1}} = \left(\frac{\partial l_i}{\partial x_i}\frac{\partial a_{i+1}}{\partial l_i} + \frac{\partial l_{i+1}}{\partial x_i}\frac{\partial a_{i+1}}{\partial l_{i+1}}\right)\frac{\partial \varphi_{i+1}}{\partial a_{i+1}} + \frac{\partial l_{i+1}}{\partial x_i}\frac{\partial b_{i+1}}{\partial l_{i+1}}\frac{\partial \varphi_{i+1}}{\partial b_{i+1}}
$$

$$
= \frac{\partial a_{i+1}}{\partial l_i}\frac{\partial \varphi_{i+1}}{\partial a_{i+1}} - \frac{\partial a_{i+1}}{\partial l_{i+1}}\frac{\partial \varphi_{i+1}}{\partial a_{i+1}} - \frac{\partial b_{i+1}}{\partial l_{i+1}}\frac{\partial \varphi_{i+1}}{\partial b_{i+1}} = \frac{\partial a_{i+1}}{\partial l_i}\frac{\mathbf{a}_{i+1} \times (\mathbf{a}_{i+1} \times \mathbf{b}_{i+1})}{\mathbf{a}_{i+1}{}^2 |\mathbf{a}_{i+1} \times \mathbf{b}_{i+1}|} - \frac{\mathbf{u}_{i+1} \times \mathbf{u}_i}{l_{i+1} \sin \beta_i \tan \beta_i} + \frac{\mathbf{u}_{i+1} \times \mathbf{u}_{i+2}}{l_{i+1} \sin \beta_{i+1} \tan \beta_{i+1}}
$$

$$
= (\mathbf{l}_{i+1} \mathbf{l}_{i+1}{}^T - \mathbf{l}_{i+1}{}^T \mathbf{l}_{i+1})\frac{\mathbf{l}_{i+1} \times \mathbf{l}_i}{l_{i+1}{}^3 l_i{}^2 \sin^2 \beta_i} - \frac{\mathbf{u}_{i+1} \times \mathbf{u}_i}{l_{i+1} \sin \beta_i \tan \beta_i} + \frac{\mathbf{u}_{i+1} \times \mathbf{u}_{i+2}}{l_{i+1} \sin \beta_{i+1} \tan \beta_{i+1}}
$$

$$
= -\frac{\mathbf{l}_{i+1} \times \mathbf{l}_i}{l_{i+1} l_i{}^2 \sin^2 \beta_i} - \frac{\mathbf{u}_{i+1} \times \mathbf{u}_i}{l_{i+1} \sin \beta_i \tan \beta_i} + \frac{\mathbf{u}_{i+1} \times \mathbf{u}_{i+2}}{l_{i+1} \sin \beta_{i+1} \tan \beta_{i+1}} = -\frac{\mathbf{u}_{i+1} \times \mathbf{u}_i}{l_i \sin^2 \beta_i} - \frac{\mathbf{u}_{i+1} \times \mathbf{u}_i}{l_{i+1} \sin \beta_i \tan \beta_i} + \frac{\mathbf{u}_{i+1} \times \mathbf{u}_{i+2}}{l_{i+1} \sin \beta_{i+1} \tan \beta_{i+1}},
$$

$$
\tag{43}
$$

$$
\frac{\partial \varphi_{i+2}}{\partial \mathbf{x}_i} = \frac{\partial \mathbf{a}_{i+2}}{\partial \mathbf{x}_i}\frac{\partial \varphi_{i+2}}{\partial \mathbf{a}_{i+2}} = \frac{\partial \mathbf{l}_{i+1}}{\partial \mathbf{x}_i}\frac{\partial \mathbf{a}_{i+2}}{\partial \mathbf{l}_{i+1}}\frac{\partial \varphi_{i+2}}{\partial \mathbf{a}_{i+2}} = -\frac{\partial \mathbf{a}_{i+2}}{\partial \mathbf{l}_{i+1}}\frac{\partial \varphi_{i+2}}{\partial \mathbf{a}_{i+2}} = \frac{\mathbf{u}_{i+2} \times \mathbf{u}_{i+1}}{l_{i+1} \sin^2 \beta_{i+1}},
$$

$$
\tag{44}
$$

$$
\frac{\partial \varphi_{i-1}}{\partial \mathbf{x}_i} = \frac{\partial \mathbf{b}_{i-1}}{\partial \mathbf{x}_i}\frac{\partial \varphi_{i-1}}{\partial \mathbf{b}_{i-1}} = \frac{\partial \mathbf{l}_i}{\partial \mathbf{x}_i}\frac{\partial \mathbf{b}_{i-1}}{\partial \mathbf{l}_i}\frac{\partial \varphi_{i-1}}{\partial \mathbf{b}_{i-1}} = \frac{\partial \mathbf{b}_{i-1}}{\partial \mathbf{l}_i}\frac{\partial \varphi_{i-1}}{\partial \mathbf{b}_{i-1}} = \frac{\mathbf{u}_{i-1} \times \mathbf{u}_i}{l_i \sin^2 \beta_{i-1}}.
$$

$$
\tag{45}
$$

Thus

$$
\mathbf{F}_i{}^t = \underbrace{-\frac{k^t \psi_{i-1}}{l_i \sin \beta_{i-1}}\frac{\mathbf{u}_{i-1} \times \mathbf{u}_i}{\sin \beta_{i-1}}}_{F_i{}^{t,i-1}} + \underbrace{\frac{k^t \psi_i}{l_{i+1} \sin \beta_i}\frac{\mathbf{u}_i \times \mathbf{u}_{i+1}}{\sin \beta_i}}_{F_i{}^{t,i,1} = -F_{i+1}{}^{t,i}} + \underbrace{\frac{k^t \psi_i}{l_i \tan \beta_i}\frac{\mathbf{u}_i \times \mathbf{u}_{i+1}}{\sin \beta_i}}_{F_i{}^{t,i,2} = -F_{i-1}{}^{t,i,3}} + \underbrace{\frac{k^t \psi_i}{l_i \tan \beta_{i-1}}\frac{\mathbf{u}_{i-1} \times \mathbf{u}_i}{\sin \beta_{i-1}}}_{F_i{}^{t,i,3} = -F_{i-1}{}^{t,i,2}}
$$

$$
- \underbrace{\frac{k^t \psi_{i+1}}{l_i \sin \beta_i}\frac{\mathbf{u}_i \times \mathbf{u}_{i+1}}{\sin \beta_i}}_{F_i{}^{t,i+1,1}} - \underbrace{\frac{k^t \psi_{i+1}}{l_{i+1} \tan \beta_i}\frac{\mathbf{u}_i \times \mathbf{u}_{i+1}}{\sin \beta_i}}_{F_i{}^{t,i+1,2}} - \underbrace{\frac{k^t \psi_{i+1}}{l_{i+1} \tan \beta_{i+1}}\frac{\mathbf{u}_{i+1} \times \mathbf{u}_{i+2}}{\sin \beta_{i+1}}}_{F_i{}^{t,i+1,3}} + \underbrace{\frac{k^t \psi_{i+2}}{l_{i+1} \sin \beta_{i+1}}\frac{\mathbf{u}_{i+1} \times \mathbf{u}_{i+2}}{\sin \beta_{i+1}}}_{F_i{}^{t,i+2}}.
$$

$$
\tag{46}
$$

Appendix B. Supplementary data

Supplementary data associated with this article can be found, in the online version, at http://dx.doi.org/10.1016/j.jmsy.2017.02.001.

References

[1] Mikchevitch A, Léon J-C, Gouskov A. Flexible beam part manipulation for assembly operation simulation in a virtual reality environment. J Comput Inf Sci Eng 2004;4:114–23.

[2] PingJun X, Lopes A, Restivo M, YingXue Y. A new type haptics-based virtual environment system for assembly training of complex products. Int J Adv Manuf Technol 2012;58:379–96.

[3] Johansen V. Modelling of flexible slender systems for real-time simulation and control applications. Norwegian University of Science and Technology; 2007. Doctoral Dissertation.

[4] Ng FM, Ritchie JM, Simmons JEL, Dewar RG. Designing cable harness assemblies in virtual environments. J Mater Process Technol 2000;107:37–43.

[5] Ng FM, Ritchie JM, Simmons JEL. The design and planning of cable harness assemblies. Proc Inst Mech Eng Part B J Eng Manuf 2000;214:881–90.

[6] Ritchie JM, Robinson G, Day PN, Dewar RG, Sung RCW, Simmons JEL. Cable harness design, assembly and installation planning using immersive virtual reality. Virtual Real 2007;11:261–73.

[7] Valentini PP. Interactive cable harnessing in augmented reality. Int J Interact Des Manuf 2011;5:45–53.

[8] Liu Y, Li SQ, Wang JF. Interactive operation of physically-based slender flexible parts in an augmented reality environment. Sci China Technol Sci 2014;57:1383–91.

[9] Jiménez P. Survey on model-based manipulation planning of deformable objects. Robot Comput Integr Manuf 2012;28:154–63.

[10] Terzopoulos D, Qin H. Dynamic NURBS with geometric constraints for interactive sculpting. ACM Trans Graph 1994;13:103–36.

[11] Lenoir J, Cotin S, Duriez C, Neumann P. Interactive physically-based simulation of catheter and guidewire. Comput Graph 2006;30:416–22.

[12] Lenoir J, Grisoni L, Chaillou C. Meseure PBT-GC. adaptive resolution of 1D mechanical B-spline. Graph. Conf 2005:395–403.

[13] Theetten A, Grisoni L, Andriot C, Barsky B. Geometrically exact dynamic splines. Comput Aided Des 2008;40:35–48.

[14] Valentini PP, Pennestrì E. Modeling elastic beams using dynamic splines. Multibody Syst Dyn 2011;25:271–84.

[15] Brown J, Latombe JC, Montgomery K. Real-time knot-tying simulation. Vis Comput 2004;20:165–79.

[16] Redon S, Galoppo N, Lin MC. Adaptive dynamics of articulated bodies. ACM Trans Graph 2005;24:936–45.

[17] Hergenröther E, Dähne P. Real-time virtual cables based on kinematicsimulation; 2000.

[18] Servin M, Lacoursiere C. Rigid body cable for virtual environments. IEEE Trans Vis Comput Graph 2008;14:783–96.

[19] Aristidou A, Lasenby J. FABRIK: a fast, iterative solver for the Inverse Kinematics problem. Graph Models 2011;73:243–60.

[20] Kaufmann P, Martin S, Botsch M, Gross M. Flexible simulation of deformable models using discontinuous Galerkin FEM. Graph Models 2009;71:153–67.

[21] Abed NY, Mohammed OA. Frequency-dependent coupled field-circuit modeling of armored power cables using finite elements. IEEE Trans Magn 2011;47:930–3.

[22] Kirchhoff G. Ueber das gleichgewicht und die bewegung eines unendlich dünnen elastischen stabes. J Für Die Reine Und Angew Math 1859;56:285–313.

[23] Bertails F, Audoly B, Cani M-P, Querleux B, Leroy F, Leroy J-L. Super-helices for predicting the dynamics of natural hair. ACM Trans Graph 2006;25:1180–7.

[24] Bergou M, Wardetzky M, Robinson S, Audoly B, Grinspun E. Discrete elastic rods. ACM Trans Graph 2008;27:63 (12 pp.).

[25] Bretl T, McCarthy Z. Quasi-static manipulation of a Kirchhoff elastic rod based on a geometric analysis of equilibrium configurations. Int J Robot Res 2014;33:48–68.

[26] Pai DK. Strands: interactive simulation of thin solids using cosserat models. Comput Graph Forum 2002;21:347–52. Wiley Online Library.

[27] Spillmann J, Teschner M. CORDE: cosserat rod elements for the dynamic simulation of one-dimensional elastic objects. Proc ACM Siggraph 2007;6:3–7, 2.

[28] Grégoire M, Schömer E. Interactive simulation of one-dimensional flexible parts. Comput Aided Des 2007;39:694–707.

[29] Provot X. Deformation constraints in a mass-spring model to describe rigid cloth behavior. Proc Graph Interface Conf 1995:147–54.

[30] ElBadrawy AA, Hemayed EE. Speeding up cloth simulation by linearizing the bending function of the physical mass-spring model. Int. Conf. 3D Imaging, Model. Process. Vis. Transm. (3DIMPVT) 2011:101–7.

[31] Patete P, Iacono MI, Spadea MF, Trecate G, Vergnaghi D, Mainardi LT, et al. A multi-tissue mass-spring model for computer assisted breast surgery. Med Eng Phys 2013;35:47–53.

[32] Selle A, Lentine M, Fedkiw R. A mass spring model for hair simulation. ACM Trans Graph 2008;27:64 (11 pp.).

[33] Haumann DR, Parent RE. The behavioral test-bed: obtaining complex behavior from simple rules. Vis Comput 1988;4:332–47.

[34] Loock A, Schömer E, Stadtwald I. A virtual environment for interactive assembly simulation: from rigid bodies to deformable cables. 5th World Multiconf Syst Cybern Inform 2001;3:325–32.

[35] van den Bergen G. Efficient collision detection of complex deformable models using AABB trees. J. Graph. Tools 1997;2:1–13.

[36] Gottschalk S, Lin MC, Manocha D. OBBTree: a hierarchical structure for rapid interference detection. In: Proc. 23rd Annu. Conf. Comput. Graph. Interact. Tech. 1996. p. 171–80.

[37] Agarwal P, Guibas L, Nguyen A, Russel D, Zhang L. Collision detection for deforming necklaces. Comput Geom 2004;28:137–63.

[38] Klosowski JT, Held M, Mitchell JSB, Sowizral H, Zikan K. Efficient collision detection using bounding volume hierarchies of k-DOPs. IEEE Trans Vis Comput Graph 1998;4:21–36.

[39] Ehmann SA, Liu MC. Accurate and fast proximity queries between polyhedra using convex surface decomposition. Comput Graph Forum 2001;20:500–10.

[40] Xu H, Zhao Y, Barbic J. Implicit multibody penalty-based distributed contact. IEEE Trans Vis Comput Graph 2014;20:1266–79.